ORIGINAL RESEARCH ARTICLE

A Study on Microstructure and Mechanical Properties of Electron Beam Welded Joint of Nb/Selective Laser-Melted TC4 Dissimilar Alloys

Yulong Li, Yuchen Meng, Min Lei, Wenqin Wang, and Xuewen Li

In this work, high-quality welding of two dissimilar Nb/TC4 and Nb/SLMed TC4 alloys is performed via electron beam welding. The precise control over orthogonal parameter optimization built strong mechanical performance of Nb/SLMed TC4 welded joints. The optimal conditions for attaining the highest tensile strength of 314.1 MPa are 62 kV of acceleration voltage, 10 mA of welding beam current, and 4.5 mm/s of scanning rate. The tensile strength of Nb/TC4 joint can be modulated by applied welding beam current, followed by acceleration voltage and scanning rate. Welded surfaces are investigated for crystal phase and microstructure analysis. Notably, no intermetallic compounds are formed in the fusion zone (FZ), and a dendritic zone of Ti-rich phase and an island zone of Nb-rich phase are observed for all welded joints. Results confirmed that composition segregation occurs in the Nb/TC4 and Nb/SLMed TC4 dissimilar joints.

1. Introduction

A substantial volume of reported experimental research discloses the expansion of titanium research over the past 3 decades (Ref 1). Titanium alloys as prominent structural materials are adopted in diverse industries (spanning from aerospace to biomedical applications) due to tunable properties: strength, ductility, toughness, and fatigue characteristics (Ref 1, 2). Lately, 3D printing technology via titanium-based 3D printing materials has given reliable outcomes in aerospace, biomedical, and automotive applications. For instance, the selective laser-melted (SLMed) TC4 can provide commendable strength and ductility (Ref 3, 4) through optimized printing parameters and heat treatments. Typically, the manufacturing process includes joint of various dissimilar metals, which forms thick brittle intermetallic compounds during the welding between titanium alloys and most different metals, deteriorating the quality of joints. To address, niobium (Nb: high melting point) metal as a transitional layer can enhance the quality of joints. It strengthens a high-quality joint between SLMed TC4 and dissimilar metals.

Yulong Li, Yuchen Meng, and **Min Lei**, Key Lab for Robot and Welding Automation of Jiangxi Province, School of Advanced Manufacturing, Nanchang University, Nanchang 330031, China; **Wenqin Wang**, School of Advanced Manufacturing, Nanchang University, Nanchang 330031, China; and **Xuewen Li**, The Engineering Training Center of Nanchang University, Mechanical and Electrical Engineering School, Nanchang University, Nanchang 330031, China. Contact e-mail: lixuewen@ncu.edu.cn.

Possesses physical and chemical properties similar to those of conventional TC4 material. During high-temperature welding, the grain size at the welded joint tends to grow due to inadequate thermal conductivity of TC4, diminishing the weld plasticity (Ref 5). M. Sabzi (Ref 6) used the gas-tungsten arc welding (GTAW) of 316L/310S joint via continuous and pulsed mode current, which transformed the columnar dendrites to the very fine equiaxed dendrites, thereby improving the mechanical properties of welded joints. The electromagnetic vibration can alter the weld quality of 316L steel; the shrinkage in grain size refines mechanical behavior (Ref 6). Consequently, there is an ongoing need for continuous improvement in the welding processes employed for TC4. In scenarios involving intricate structures, the fusion welding techniques, such as laser beam welding (LBW) and electron beam welding (EBW), can be used for joining TC4 with dissimilar metals. Gu et al. (Ref 7) applied laser welding to join Ti and Al components with Nb transition layer, which enabled a barrier composed of (Ti, Nb) solid solution between TC4 and 6082 aluminum alloys, preventing the formation of brittle TiAl, TiAl$_2$, and TiAl$_3$ phases. Mota Siqueira et al. (Ref 8) welded a niobium titanium plate by fiber laser beam; the globular dissolution and mass flow around the keyhole allowed the homogenization of the weld bead. Lei et al. (Ref 9) investigated the microstructural evolution of Ti-22Al-27Nb/TC4 dissimilar joint by LBW; the results showed that the FZ consisted of martensitic α' and B2 phases. Torkamany et al. (Ref 10-12) performed dissimilar butt welding of pure niobium plate to the titanium alloy Ti-6Al-4 V sheet using a pulsed Nd: YAG laser and established suitable welding process parameters. Hao et al. (Ref 13) used the filler material of (FeCoCrNi)$_{100-x}$Cu$_x$ to achieve the joining of TC4 alloy and 304 stainless steel. M-anucci et al. (Ref 14) employed vanadium as an intermediate layer, restricting the formation of intermetallic compounds (IMCs) during laser welding, and reported improved mechanical performance of TC4/316L welding joints. Gao et al. (Ref 15) mentioned the pulsed laser welding-induced eutectic reaction technology by

welding Ti6Al4V and Inconel 718 through pulsed laser welding and selected niobium as an interlayer. Nb as an interlayer avoided mixing of Ti6Al4V alloy with Inconel 718, which prevented Ti-Ni, Ti-Cr, and Ti-Fe brittle intermetallics. In contrast to laser welding, vacuum electron beam welding can prevent the impact of atmospheric conditions on weld quality under a controlled vacuum environment. Mo et al. (Ref 16) established dissimilar metal joints using Cu/Nb multilayer interlayers between TC4 and Kovar alloy by electron beam welding. High welding speed agglomerated (Nb, Ti) solid solution on the titanium alloy, and the formation of brittle FeTi is effectively suppressed. Pederson et al. (Ref 17) used electron beam welding of TC4 and Ti-6Al-2Sn-4Zr-6Mo titanium alloys with different thickness and reported tensile strength and yield strength values within the established standard range. Parise et al. (Ref 18) developed a new type of electron beam welded joint using Nb and 2 titanium grades. This allows to join directly the most used materials of superconducting radio frequency cavities. Furthermore, the tensile and creep properties of the joints remain intact after the post-weld heat treatment. In addition, researchers (Ref 19-22) have investigated the microstructure and mechanical properties of welds produced through electron beam welding of TC4.

The reported studies have been lacking in optimizing of welding parameters of TC4 welded joints with dissimilar metals. Jing et al. (Ref 23, 24) achieved smooth macroscopic forming and good metallurgical bonding of TC4/AlSi12 bimetallic structure (BS) through laser additive manufacturing (LAM) technology and parameter optimization. The incorporation of a niobium (Nb) interlayer formed an element diffusion barrier, which inhibited the formation of intermetallic compounds (IMCs) and improved the tensile strength of TC4/AlSi12 bimetallic structure. Sainand et al. (Ref 25, 26) investigated the microstructures and mechanical properties of BS of a titanium alloy (Ti6Al4V) and a niobium alloy (NbZr1) manufactured by wire arc additive manufacturing (WAAM), demonstrating the feasibility of fabricating Ti6Al4V-NbZr1 BS by WAAM. At present, research on the welding of SLMedTC4 with dissimilar metals has been lacking. Researchers have achieved joints between traditional TC4 and dissimilar metals through various joining methods, but there is limited research on the joining SLMed TC4 and dissimilar metals. As reported, a transition layer of Nb can refine the quality of joints between titanium alloys and dissimilar metals; it plays immense significance in enhancing the joint quality of SLMed TC4 with dissimilar metals.

In this study, the process parameters for electron beam welding of conventional TC4 and Nb are optimized. Subsequently, SLMed TC4 and Nb welding are carried out at the optimized process parameters. The resulting welds are subjected to analysis of internal microstructure evolution, element distribution, and mechanical properties. This study offers a theoretical foundation and novel insights for achieving reliable joints between SLMed TC4 and various dissimilar metals.

2. Experimental Materials and Methods

The chemical compositions of the base metal (wt.%) were as follows: TC4 (Ti-89.79, Al-6.15, V-4.06); SLMedTC4 (Ti-90.63, Al-5.53, V-3.84); Nb (>99.95). The microstructure of the three base metals is shown in Fig. 1. TC4 alloy consists of equiaxed α phase and granular β phase microstructures, and the equiaxed grains are observed in the niobium alloy. The structure of the net basket is seen in the cross section of SLMedTC4 base metals.

Herein, a flat butt joint welding configuration was adopted with the welding piece size of $50 \times 20 \times 1$ mm (thickness). Before welding process, the mating surface and its surrounding area were ground to remove the oxides and thoroughly cleaned with acetone to eliminate contaminants such as oil and dust particles.

Upon the completion of the welding process, samples were collected by wire cutting. Thereafter, specimens were taken from the welded joint and prepared for tensile and metallographic testing. The specimen with a size of $40 \times 8 \times 1$ mm was selected for tensile testing. For metallographic analysis, specimen with a size of $10 \times 10 \times 1$ mm was ground with sandpaper to make a smooth surface.

Preparatory measures were executed on the metallographic specimen, and the observation side was oriented downward and embedding. Subsequent to embedding, the samples were polished using sandpaper of #600, #1000, #1500, and #2000 in sequence, followed by a final polishing procedure using a polishing apparatus. The polished samples were corroded using Kroll reagent (1-3 mL HF; 2-6 mL HNO_3; 100 mL H_2O). The conditions and standards used for metallography followed GB/T 13298-2015. The microstructure, phase, and surface analysis were conducted employing an x-ray diffractometer, optical microscope, and scanning electron microscope. The tensile strength evaluation of the joint was performed using a microcomputer (CTM2500) controlled electronic universal testing machine under the regulation of GB-T 228.1-2021. The final testing value was the average of 3 times.

3. Results and Discussion

3.1 Parameter Optimization Test

The heat input during the electron beam welding process primarily depends on the acceleration voltage and welding beam current. The quality of welding joints can be modulated through accelerating voltage, welding beam, and scanning rate. The high accelerating voltage and intense welding beam can penetrate the weld, and low scanning rate can melt the base metal, which spreads the cross section of weld, leading to enhanced penetration and compromised joint quality.

Based on the magnitude of F value, an initial assessment of the relative significance of the factors is carried out to explore the impact of these on the quality of the joint (Tables 1 and 2). The sequence of factors affecting joint quality is determined as follows: welding beam current > acceleration voltage > scanning rate (Ref 27). During the welding process, optimal process parameters were evaluated. The highest tensile strength is observed at 62 kV of acceleration voltage, 10 mA of welding beam current, and 4.5 mm/s of scanning rate.

3.2 Cross Sections of the Weld Joints

Optical images of the cross sections were analyzed for 9 different parameters of the welded joints, and the cross-sectional morphology and microstructure of each welded joint are shown in Fig. 2.
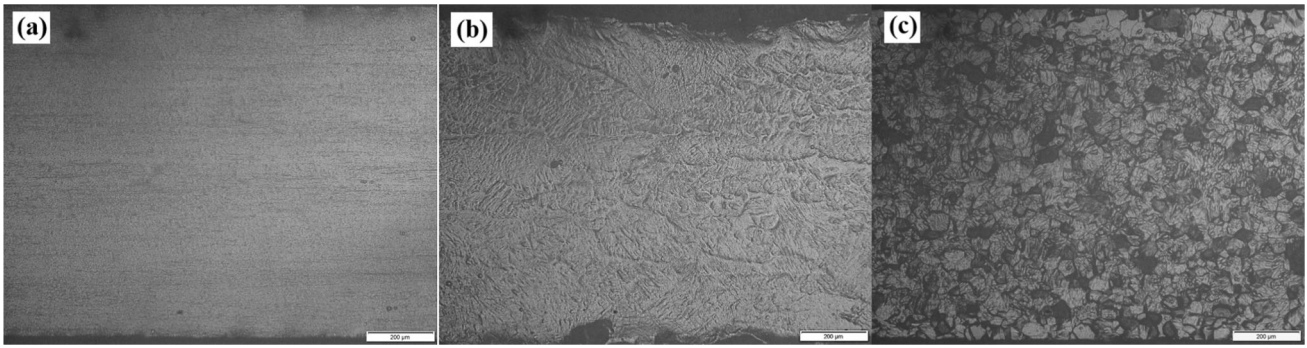
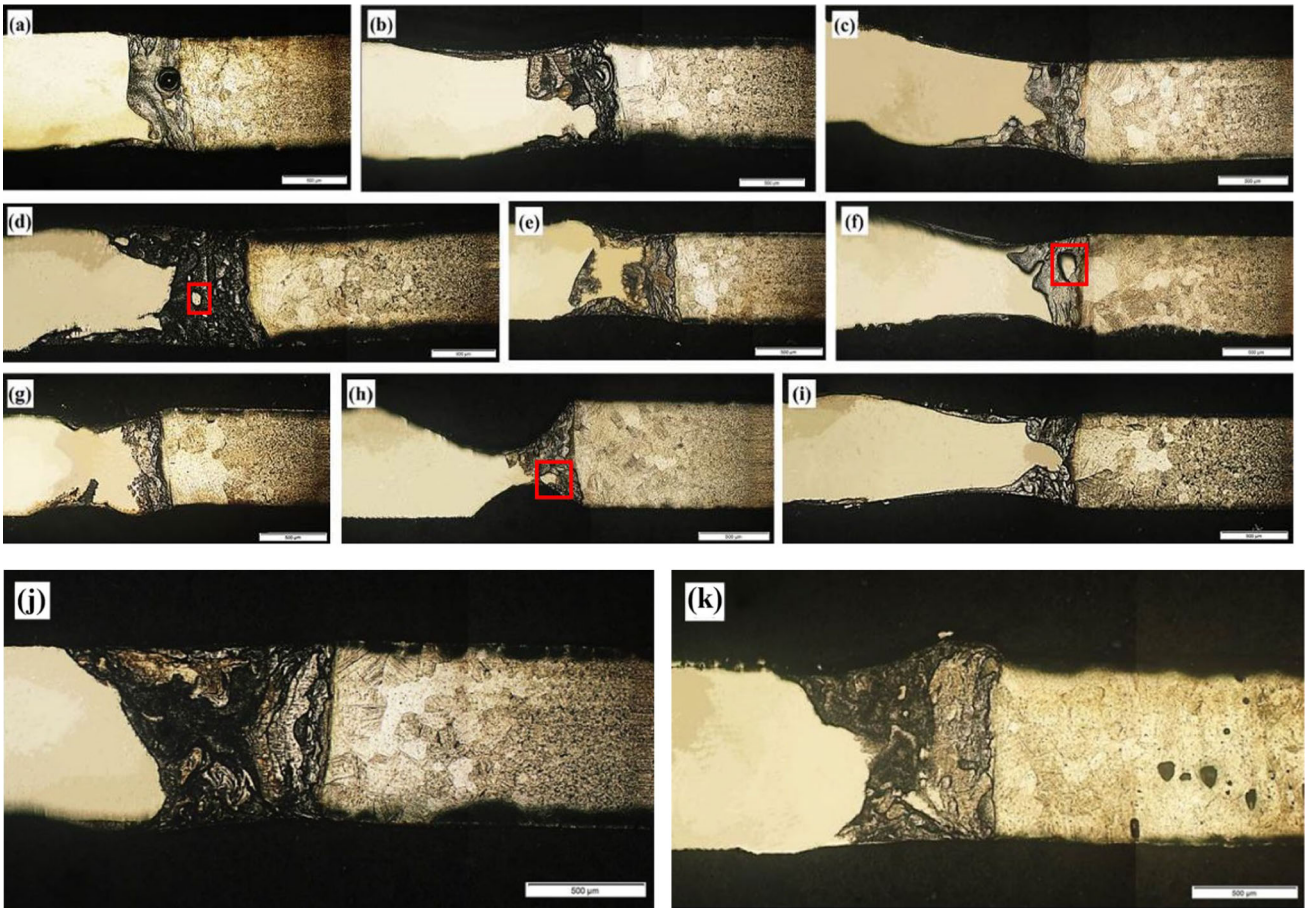**Fig. 1** The microstructure of the base material (a) TC4; (b) SLMedTC4; (c) Nb

Fig. 2 Cross section of Nb/TC4 joints with different parameters: (a) 62Kv, 8 mA, 4.5 mm/s; (b) 62Kv, 10 mA, 4.2 mm/s; (c) 62Kv, 12 mA, 3.8 mm/s; (d) 65Kv, 8 mA, 4.2 mm/s; (e) 65Kv, 10 mA, 3.8 mm/s; (f) 65Kv, 12 mA, 4.5 mm/s; (g) 68Kv, 8 mA, 3.8 mm/s; (h) 68Kv, 10 mA, 4.5 mm/s; (i) 68Kv, 12 mA, 4.2 mm/s; Joint cross-sectional morphology with optimal parameters: (j) Nb/TC4 with parameters of 62 kV, 10 mA, 4.5 mm/s; (k) Nb/SLMedTC4 with parameters of 62 kV, 10 mA, 4.5 mm/s

In Fig. 2(a), and (c), the distribution of various sizes of pores is observed on the cross sections of the specimens. The formation of smaller size pores is caused by insufficient heat input (Fig. 2c), resulting in insufficient mixing of the molten pool. From Fig. 2h, the variation in the thickness of cross section occurs due to the large heat input caused by applied parameters. The phenomenon of partial penetration of the weld appeared, and the thickness of the weld is uneven. The cross section in Fig. 2h is at the part of the thinner thickness of the weld, so the thickness has significantly changed compared with

other figures. There are discernible structures resembling small islands, highlight in Fig. 2(d), (f), and (h), this may be caused by macrosegregation (Ref 28, 29). The contrast of protruding structures differs significantly from the surrounding weld seam, and it exhibits a distinguishable contrast of Nb base metal. Preliminary analysis indicates that these small pieces correspond to Nb-rich phases.

Nb/TC4 and Nb/SLMed TC4 were joined using optimized parameters, and the morphology and microstructure of the joint cross section are shown in Fig. 2(j), and (k). The weld seam

exhibits a funnel-shaped morphology. Compared to Nb side, the surface of TC4 shows a greater degree of melting. No notable defects are observed within the weld seam. Furthermore, a more uniform microstructure is formed at optimal process parameters in the welded structure, i.e., precise optimization occurs.

The formation of the weld seam in the joint between SLMed TC4 and Nb exhibits a similar pattern to that of TC4/Nb joint. However, SLMed TC4 base material displays pores with different sizes. The rationale behind the formation of pores in SLMed objects can be attributed to the strong reverse stamping caused by the rapid evaporation of the metal during laser melting. It pushes the surrounding molten liquid downward, creating deep and narrow cavities called keyholes. The laser beam is reflected several times in the keyhole, which in turn enhances the laser absorption, resulting in improved energy conversion efficiency. It is noteworthy that the keyhole wall constantly fluctuates and collapses under certain laser conditions. It can be caused by the complex interaction of thermal capillary forces, Marangoni convection, recoil pressure, and the production of gas plasma. This unstable state of keyholes creates pores (Ref 30). 3D printing is a stratified process, and each layer undergoes different cooling rates, implying that pore generation is inevitable (Ref 31, 32).

The surface morphology of the joint was examined using a scanning electron microscope, and the weld section is shown in Figs. 3 and 4.

It can be seen that the formation of Nb/SLMed TC4 joint closely resembles weld seam of Nb/TC4 joint, and the weld seam possesses blocky structures. The nonuniform distributions of the mixing elements in Nb and TC4 are observed in the molten pool during electron beam welding. The uneven distribution of elements is caused by the Marangoni currents (Ref 33, 34).

As shown in Fig. 5, Nb/SLMedTC4 weld section exhibits a slightly lower hardness as compared to Nb/TC4 weld section. This disparity may arise from the fact that the hardness of SLMedTC4 is lower than that of TC4.

To get insight into the distribution of elements in the weld seam, EDS and XRD studies were performed on the weld seam area. The elemental mapping outcomes are shown in Tables 3 and 4. The element distribution of Nb/SLMed TC4 joint weld seam is similar to that of Nb/TC4 joint, and the block structure primarily consists of Ti and Nb elements as observed in the weld seam. No intermetallic compounds are formed in the FZ. By combining points B, C, D, H, and I in Fig. 3 and Table 3, Ti content in the molten pool near Nb side is higher than Nb content in the molten pool near the TC4 side. It can be inferred that the diffusion of Ti atoms to Nb side is faster than that of Nb atoms to TC4 side. A dendritic zone of Ti-rich phases and an island zone of Nb-rich phases are observed for welded joints, i.e., the composition segregation occurred in Ti6Al4V/Nb dissimilar joint. Furthermore, the element proportion of the (Ti, Nb) solid solution formed by Nb and Ti in the welding process is not consistent (Ref 35), leading to the formation of nonuniform regions in the weld.

Based on the crystal phase analysis, the weld seam primarily consists of a composition of β-Ti phase and (β-Ti, Nb) solid solution (Fig. 6). β-Ti phase is predominant in the weld seam, as the temperature in the electron beam welding process exceeds β transition temperature of TC4. It allows transformation of α-Ti alloy into β-Ti, and β-Ti and Nb form a (β-Ti, Nb) solid solution in the welding process. The presence of Nb hinders the transformation process of β-Ti to α-Ti. Combined with the results of XRD and SEM, it can also be confirmed that the weld contains a large amount of β-Ti.

Additionally, the presence of Nb hinders the transformation process of β-Ti phase to α-Ti. The presence of β-Ti stimulates
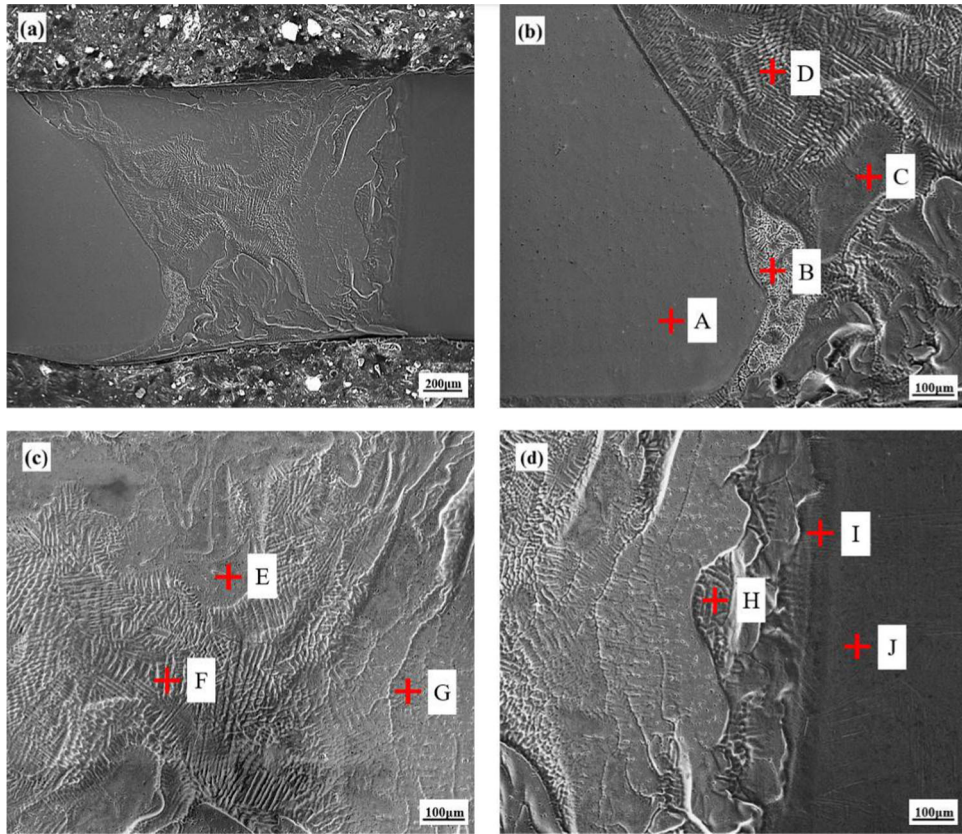
Table 1 Orthogonal test plan for electron beam welding

Factor	A	B	C	e	Protocol
1	62	8	4.5	1	$A_1B_1C_1$
2	62	10	4.2	2	$A_1B_2C_2$
3	62	12	3.8	3	$A_1B_3C_3$
4	65	8	4.2	3	$A_2B_1C_2$
5	65	10	3.8	1	$A_2B_2C_3$
6	65	12	4.5	2	$A_2B_3C_1$
7	68	8	3.8	2	$A_3B_1C_3$
8	68	10	4.5	3	$A_3B_2C_1$
9	68	12	4.2	1	$A_3B_3C_2$

Table 2 Orthogonal test conditions and results

Specimen nos	Voltage, kV	Current, mA	Scanning rate, mm/s	Error column	Tensile strength, MPa
1	62	8	4.5	1	286.7
2	62	10	4.2	2	290.3
3	62	12	3.8	3	280.6
4	65	8	4.2	3	249.4
5	65	10	3.8	1	288.4
6	65	12	4.5	2	257.5
7	68	8	3.8	2	215.1
8	68	10	4.5	3	286.3
9	68	12	4.2	1	255.9
K1	857.6	751.2	830.5	831.0	
K2	795.3	865.0	795.6	762.9	
K3	757.3	794.0	784.1	816.3	
K2 1	735477.76	564301.44	689730.25	690561.00	
K2 2	632502.09	748225.00	632979.36	582016.41	
K2 3	573503.29	630436.00	614812.81	666345.69	
S	1709.49	2202.59	389.25	855.91	
F	1.99	2.57	0.45		

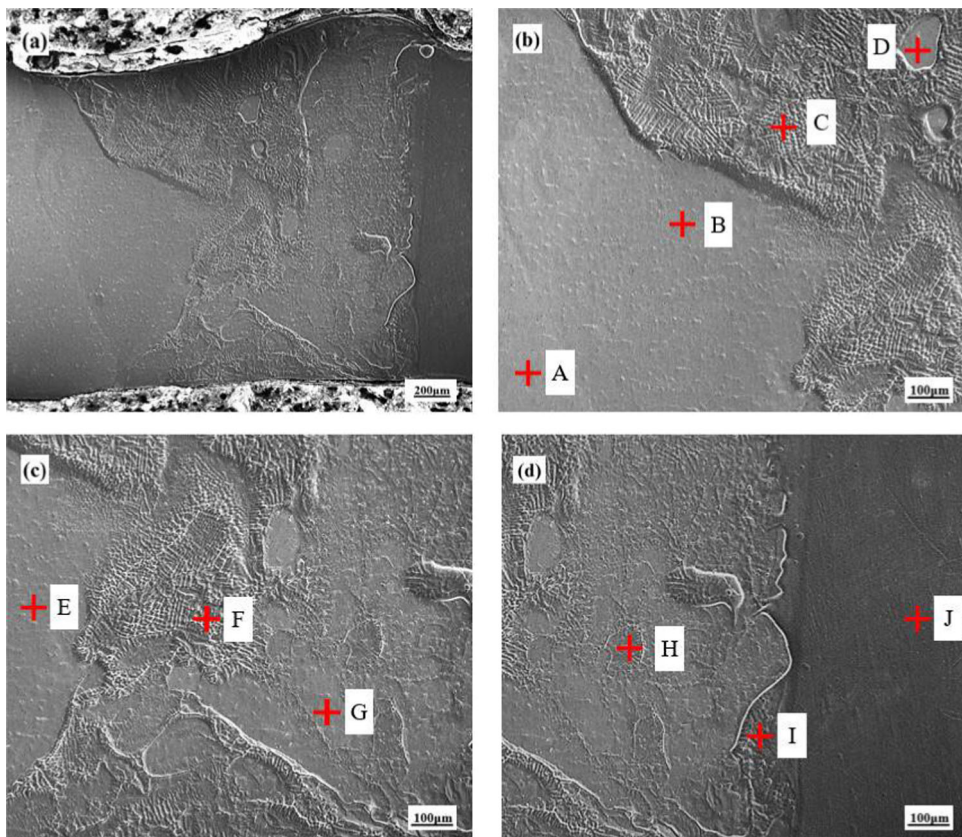**Fig. 3** Microstructures of FZ in Nb/TC4 joints

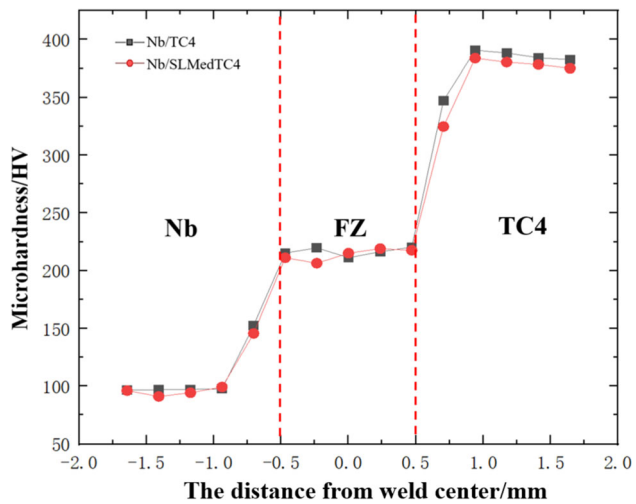**Fig. 4** Microstructure of FZ in Nb/SLMed TC4 joints

Fig. 5 Microhardness of the tested points of the weld cross section for Nb/TC4 joints and Nb/SLMedTC4 joints

Table 3 EDS results of the Nb/TC4 joints (at.%) in Fig. 3

	Ti	Al	V	Nb
A	0.16	0.23	0.03	99.58
B	54.40	5.21	3.23	37.16
C	49.61	4.24	2.79	43.36
D	64.69	6.39	3.43	25.50
E	57.67	4.18	…	38.15
F	78.08	5.41	…	16.51
G	37.31	2.93	…	59.76
H	85.36	4.48	…	10.16
I	89.72	5.73	…	4.55
J	89.79	6.23	3.98	…

Table 4 EDS results of the Nb/SLMed TC4 joints (at.%) in Fig. 4

	Ti	Al	V	Nb
A	0.26	0.13	0.08	99.53
B	35.90	2.67	1.97	59.46
C	70.30	5.28	3.89	20.52
D	29.76	3.42	1.56	65.26
E	33.67	1.85	1.97	62.51
F	69.75	4.98	4.03	21.23
G	22.82	2.04	1.42	73.73
H	57.86	6.42	3.86	31.85
I	78.85	10.25	4.97	5.93
J	85.63	10.37	3.84	0.16

the strength and ductility of the welded joints (Ref 36). The formed (β-Ti, Nb) solid solution can improve corrosion resistance and mechanical properties of the welds (Ref 36, 37).

Results indicate that the weld seam primarily consists of β-Ti and (β-Ti, Nb) solid solution. Furthermore, compared with α-Ti, β-Ti enables higher strength and plasticity, and (β-Ti, Nb) solid solution homogeneous lattice structure and solid solution
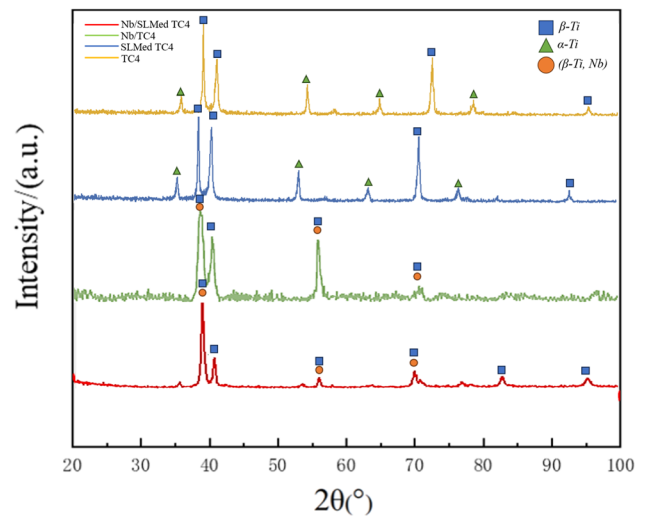

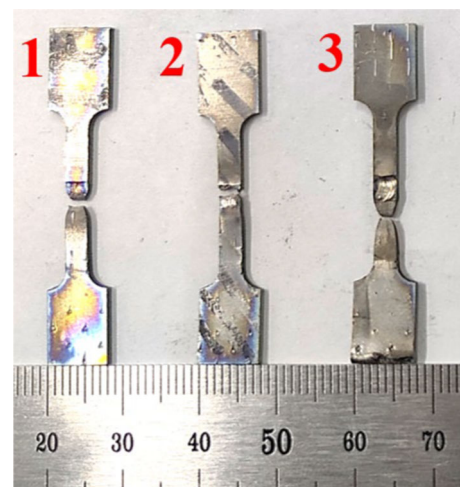Fig. 6 XRD analysis results of FZ and base meta

Fig. 7 The tensile specimens of TC4/Nb joints for parameter optimization, showing fracture failure at different locations

strengthening effect boost the deformation resistance and tensile strength of welded joints. To further validate the reliability of the joints, the welded joint is analyzed through tensile testing.

3.3 Mechanical Properties of Welded Joints

The behavior of samples underlying tensile testing is shown in Fig. 7, and the outcomes of the tensile test for each group of parameters are shown in Table 5. It can be observed that the majority of tensile specimens fracture occurs in the heat-affected zone (HAZ), and a small number of specimens exhibit fracture at the weld seam or Nb base metal. Thus, the welded joints are not reliable without parameter optimization.

In order to validate the reliability of the joint quality, tensile specimens of Nb/TC4 and Nb/SLMed TC4 joints prepared at optimal parameters are subjected to tensile strength testing. The complied outcomes are listed in Table 6, and the surface morphology of the fractured tensile specimen is shown in Fig. 8.

Table 5 Tensile test results of Nb/TC4 joints with different parameter

Specimen nos	Voltage, kV	Current, mA	Scanning rate, mm/s	Tensile strength, MPa	Fracture location
1	62	8	4.5	286.7	HAZ
2	62	10	4.2	290.3	FZ
3	62	12	3.8	280.6	Nb base metal
4	65	8	4.2	249.4	HAZ
5	65	10	3.8	288.4	HAZ
6	65	12	4.5	257.5	Nb base metal
7	68	8	3.8	215.1	HAZ
8	68	10	4.5	286.3	HAZ
9	68	12	4.2	255.9	HAZ

Table 6 Tensile test results of Nb/TC4 joints and Nb/SLMed TC4 joints

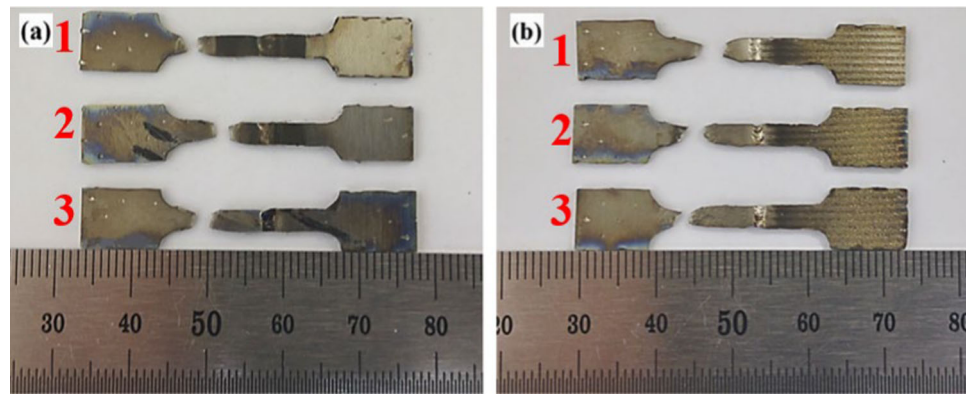| Specimen	Average elongation, %	Average tensile strength, MPa
Nb/TC4 joints	6.6 ± 1.0	314.1 ± 7.8
Nb/SLMed TC4 joints	5.2 ± 0.7	293.2 ± 0.9

Fig. 8 The tensile specimen with optimal parameters (U = 62 kV, I = 10 mA, t = 4.5 mm/s) (a) Nb/TC4; (b) Nb/SLMed TC4
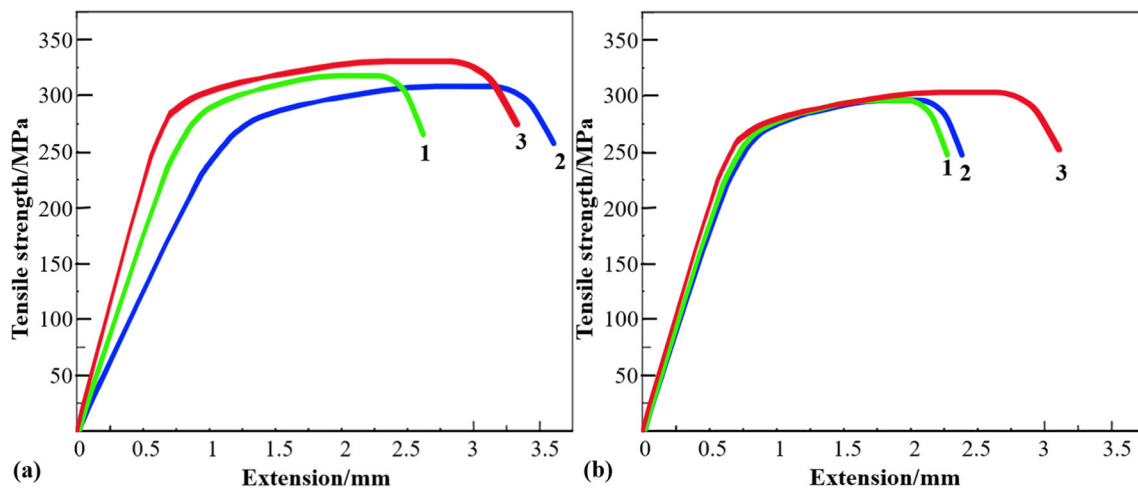

Fig. 9 Tensile curves of welded joints: (a) Nb/TC4; (b) Nb/SLMed TC4
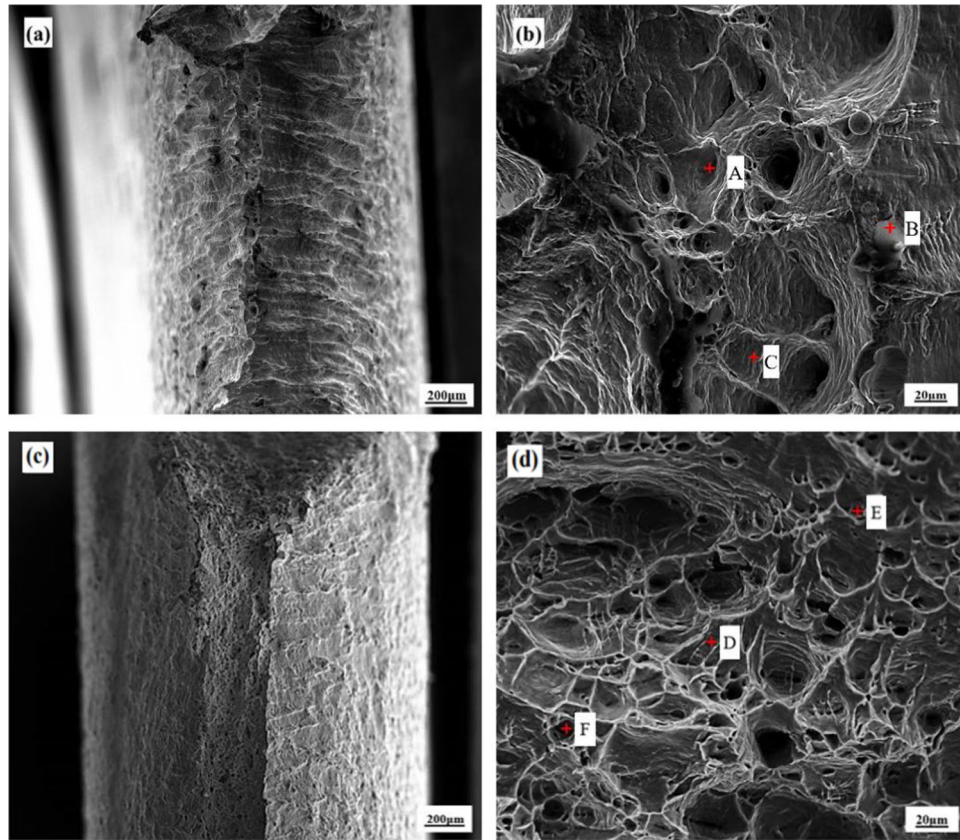
Fig. 10 Morphology of the fracture surface of the tensile specimens: (a) Nb/TC4; (c) Nb/SLMed TC4

Table 7 EDS results of fracture surface (at.%) in Fig. 10

	Ti	Al	V	Nb
A	0.49	…	…	99.51
B	0.41	0.26	…	99.33
C	0.75	…	…	99.25
D	1.00	…	0.04	98.96
E	1.18	…	…	98.82
F	1.24	0.33	…	98.43

It is evident that dissimilar joints are broken and fracture initiation took place toward Nb base metal side. A preliminary assessment indicates that the tensile strength of both the weld seam and the heat-affected zone surpasses that of Nb base metal.

Figure 9 shows the stress-strain curves of Nb/TC4 and Nb/SLMedTC4 samples. Nb/TC4 joint shows higher tensile strength as compared to Nb/SLMedTC4 joint. This may be attributed to the fact that the grain size of SLMedTC4 base metals (Fig. 1a and b) is larger than that of TC4. As reported previously, the smaller the grain size is, the higher the yield strength is (Ref 38). Compared with the sample developed without optimized parameter (Fig. 2a, b, c, d, e, f, g, h, and i), the section of Nb/SLMedTC4 joint possesses no obvious defects and a massive structure. It shows a better fusion effect, improving tensile strength.

The fracture morphologies of the welded joints are shown in Fig. 10. As can be seen, microscopic patterns show ductile dimples on the fracture surface of the welded joints. Both welded joints depict the ductile fracture pattern.

Furthermore, the fracture surface is devoid of defects such as cracks and pores. The EDS results are shown in Table 7. The outcomes of each point indicate that no other impurities are observed in Nb base metal at the fracture surface, confirming the high purity of Nb base metal within the weld seam. High purity and quality formation of weld ensure the reliability from application perspective.

Based on the aforementioned analysis, the parameter optimization plays a crucial role in enhancing the mechanical behavior of weld joints of the dissimilar metals, for instance, a significant enhancement is measured in the tensile strength of Nb/TC4 joints. The obtained process parameters are applicable to electron beam welding of Nb and SLMed TC4. The tensile strength of both Nb/TC4 joints and Nb/SLMed TC4 joints is higher than that of Nb base metal. Thus, the precise control over process parameters allows a significant refinement in the quality of welded joints.

4. Conclusions

In summary, Nb/TC4 and Nb/SLMed TC4 dissimilar joints were prepared using electron beam welding. The orthogonal parameter optimization experiments enabled the welded joints with excellent performance. The microstructure and mechanical properties of the welded joints were investigated. Based on the experimental results, the conclusions are summarized below:

1. The welding beam current is a crucial parameter to modulate the mechanical behavior of a joint. It prominently affected the tensile strength of Nb/TC4 joint, followed by acceleration voltage and scanning rate.

2. The microstructure analysis confirmed that welded joints were devoid of any intermetallic compounds in the FZ. However, the composition segregation occurred in both Nb/TC4 and Nb/SLMed TC4 joints. The weld seam primarily consisted of β-Ti phase and (β-Ti, Nb) solid solution. It should be noted that the elemental composition of (β-Ti, Nb) solid solution is not constant, as the diffusion of Nb and Ti atoms in the solid solution was different, causing a composition gradient.

3. From tensile testing results, the joints fractured at Nb base metal side during the tensile tests demonstrated that the tensile strength of both FZ and HAZ surpasses that of the Nb base metal. The tensile strength of the welded joints was ∼ 300 Mpa. Successfully obtained Nb/SLMed TC4 welded joint with excellent mechanical properties at a lower cost.

Conflict of interest

The authors declare no conflict of interest.

References

1. C.A. Salvador, E.L. Maia, F.H. Costa, J.D. Escobar, and J.P. Oliveira, A Compilation of Experimental Data on the Mechanical Properties and Microstructural Features of Ti-Alloys, *Sci Data*, 2022, **9**(1), p 188.

2. B. Callegari, J.P. Oliveira, R.S. Coelho, P.P. Brito, N. Schell, F.A. Soldera, F. Mücklich, M.I. Sadik, J.L. García, and H.C. Pinto, New Insights Into the Microstructural Evolution of Ti-5Al-5Mo-5V-3Cr Alloy During Hot Working, *Mater. Charact.*, 2020, **162**, p 110180.

3. W. Wang, X. Xu, R. Ma, G. Xu, W. Liu, and F. Xing, The Influence of Heat Treatment Temperature on Microstructures and Mechanical Properties of Titanium Alloy Fabricated by Laser Melting Deposition, *Materials*, 2020, **13**(18), p 4087.

4. Z. Pang, Y. Liu, M. Li, C. Zhu, S. Li, Y. Wang, D. Wang, and C. Song, Influence of Process Parameter and Strain Rate on the Dynamic Compressive Properties of Selective Laser-Melted Ti-6Al-4V Alloy, *Appl. Phys. A*, 2019, **125**(1), p 12.

5. F. Weng, C. Chen, and H. Yu, Research Status of Laser Cladding on Titanium and Its Alloys: A Review, *Mater. Des.*, 2014, **58**(6), p 412–425.

6. M. Sabzi, S.M. Anijdan, A.B. Chalandar, N. Park, H.R. Jafarian, and A.R. Eivani, An Experimental Investigation on the Effect of Gas Tungsten Arc Welding Current Modes Upon the Microstructure, Mechanical, and Fractography Properties of Welded Joints of Two Grades of AISI 316L and AISI310S Alloy Metal Sheets, *Mater. Sci. Eng. A*, 2022, **840**, p 142877.

7. X. Gu, M. Cui, J. Chen, D. Sun, X. Gu, and L. Liu, Laser Welding of 6082 Aluminum Alloy to TC4 Titanium Alloy Via Pure Niobium as a Transition Layer, *J. Market. Res.*, 2021, **13**(2202), p 2209.

8. R.H. de Mota Siqueira, I. Atilio, C.C. de Andrade Ferreira, S.M. De Carvalho, and M.S.F. De Lima, Fiber Laser Beam Welding Between Niobium and Titanium, *J. Aircr. Spacecr. Technol.*, 2020, **4**(1), p 21–25.

9. Z.L. Lei, Z.J. Dong, Y.B. Chen, L. Huang, and R.C. Zhu, Microstructure and Mechanical Properties of Laser Welded Ti–22Al–27TC4/Nb Dissimilar Alloys, *Mater. Sci. Eng. A*, 2013, **559**(909), p 916.

10. M.J. Torkamany, F.M. Ghaini, and R. Poursalehi, Dissimilar Pulsed Nd: YAG Laser Welding of Pure Niobium to Ti–6Al–4V, *Mater. Des.*, 2014, **53**, p 915–920.

11. M.J. Torkamany, F.M. Ghaini, R. Poursalehi, and A.F.H. Kaplan, Combination of Laser Keyhole and Conduction Welding: Dissimilar Laser Welding of Niobium and Ti-6Al-4V, *Opt. Lasers Eng.*, 2016, **79**(9), p 15.

12. M.J. Torkamany, F.M. Ghaini, and R. Poursalehi, An Insight to the Mechanism of Weld Penetration in Dissimilar Pulsed Laser Welding of Niobium and Ti-6Al-4V, *Opt. Laser Technol.*, 2016, **79**, p 100–107.

13. X. Hao, H. Dong, Y. Xia, and P. Li, Microstructure and Mechanical Properties of Laser Welded TC4 Titanium Alloy/304 Stainless Steel Joint With $(CoCrFeNi)_{100-x}Cu_x$ High-Entropy Alloy Interlayer, *J. Alloy. Compd.*, 2019, **803**(649), p 657.

14. A. Mannucci, R. Bolot, I. Tomashchuk, A. Mathieu, E. Cicala, and S. Lafaye, On the Mechanisms Involved in the Tensile Strength of a Dissimilar Ti6Al4V/316L Laser Welded Assembly, *Metallurg. Res. Technol.*, 2021, **118**(6), p 608.

15. X.L. Gao, J. Liu, and L.J. Zhang, Dissimilar Metal Welding of Ti6Al4V and Inconel 718 Through Pulsed Laser Welding-Induced Eutectic Reaction Technology, *Int. J. Adv. Manuf. Technol.*, 2018, **96**, p 1061–1071.

16. Y.J. Fang, X.S. Jiang, D.F. Mo, T.F. Song, Z.Y. Shao, D.G. Zhu, M.H. Zhu, and Z.P. Luo, Microstructure and Mechanical Properties of Electron Beam-Welded Joints of Titanium TC4 (Ti-6Al-4V) and Kovar (Fe-29Ni-17Co) Alloys with Cu/Nb Multi-Interlayer, *Adv. Mater. Sci. Eng.*, 2018, **2018**, p 2042871.

17. R. Pederson, F. Niklasson, F. Skystedt, and R. Warren, Microstructure and Mechanical Properties of Friction- and Electron-Beam Welded Ti-6Al-4V and Ti-6Al-2Sn-4Zr-6Mo, *Mater. Sci. Eng. A*, 2012, **552**, p 555–565.

18. M. Parise, D. Passarelli, and J. Bernardini. Niobium to Titanium electron beam welding for SRF cavities (2022). arXiv preprint http://arxiv.org/abs/2209.02503

19. N. Saresh, M.G. Pillai, and J. Mathew, Investigations Into the Effects of Electron Beam Welding on Thick Ti–6Al–4V Titanium Alloy, *J. Mater. Process. Technol.*, 2007, **192**, p 83–88.

20. H. Galarraga, D.A. Lados, R.R. Dehoff, M.M. Kirka, and P. Nandwana, Effects of the Microstructure and Porosity on Properties of Ti-6Al-4V ELI Alloy Fabricated by Electron Beam Melting (EBM), *Addit. Manuf.*, 2016, **10**(47), p 57.

21. N. Hrabe and T. Quinn, Effects of Processing on Microstructure and Mechanical Properties of a Titanium Alloy (Ti-6Al-4V) Fabricated Using Electron Beam Melting (EBM), Part 2: Energy Input, Orientation, and Location, *Mater. Sci. Eng. A*, 2013, **573**, p 271–277.

22. N. Hrabe and T. Quinn, Effects of Processing on Microstructure and Mechanical Properties of a Titanium Alloy (Ti-6Al-4V) Fabricated Using Electron Beam Melting (EBM), Part 1: Distance from Build Plate and Part Size, *Mater. Sci. Eng. A*, 2013, **573**, p 264–270.

23. Z. Jing, X. Liu, L. Li, W. Wang, G. Xu, and L. Chang, Microstructure and Mechanical Properties of Transition Zone in Laser Additive Manufacturing of TC4/AlSi12 Bimetal Structure, *Mater. Res. Exp.*, 2022, **9**(1), p 016513.

24. Z. Jing, X. Liu, W. Wang, N. Xu, G. Xu, and F. Xing, Laser Additive Manufacturing of TC4/AlSi12 Bimetallic Structure Via Nb Interlayer, *Materials*, 2022, **15**(24), p 9071.

25. S. Jadhav, M.S. Bajestani, S. Islam, M.A. Karim, C.J. Kim, H.J. Lee, Y.T. Cho, and D.B. Kim, Materials Characterization of Ti6Al4V to NbZr1 Bimetallic Structure Fabricated by Wire Arc Additive Manufacturing, *Mater. Today Commun.*, 2023, **36**, p 106934.

26. C. Zhang, H. Yu, D. Sun, and W. Liu, Fabrication of Multi-Material Components by Wire Arc Additive Manufacturing, *Coatings*, 2022, **12**(11), p 1683.

27. L. Wang, Y. Che, D. Wu, H. Li, D. Sun, and X. Zhang, Orthogonal Optimization of Resistance Spot Welding Parameters and Microstructure and Mechanical Property of Aluminum Alloy/High Strength Steel Joint, *Trans. Indian Inst. Met.*, 2021, **74**(3093), p 3101.

28. J. Shen, P. Agrawal, T.A. Rodrigues, J.G. Lopes, N. Schell, J. He, Z. Zeng, R.S. Mishra, and J.P. Oliveira, Microstructure Evolution and Mechanical Properties in a Gas Tungsten Arc Welded $Fe_{42}Mn_{28}Co_{10}Cr_{15}Si_5$ Metastable High Entropy Alloy, *Mater. Sci. Eng. A*, 2023, **867**, p 144722.

29. J. Shen, R. Gonçalves, Y.T. Choi, J.G. Lopes, J. Yang, N. Schell, H.S. Kim, and JPl. Oliveira, Microstructure and Mechanical Properties of Gas Metal Arc Welded CoCrFeMnNi Joints Using a 410 Stainless Steel Filler Metal, *Mater. Sci. Eng. A*, 2022, **857**, p 144025.

30. R. Cunningham, C. Zhao, N. Parab, C. Kantzos, J. Pauza, K. Fezzaa, T. Sun, and A.D. Rollett, Keyhole Threshold and Morphology in Laser Melting Revealed by Ultrahigh-Speed x-Ray Imaging, *Science*, 2019, **363**(6429), p 849–852.

31. C. Xia, Z. Pan, J. Polden, H. Li, Y. Xu, S. Chen, and Y. Zhang, A Review on Wire Arc Additive Manufacturing: Monitoring, Control and a Framework of Automated System, *J. Manuf. Syst.*, 2020, **57**(31), p 45.

32. Y. Bao, H. Sun, X. Cai, S. Lin, and C. Chen, Effect of External Magnetic Field on the Forming, Microstructure and Property of TC4 Titanium Alloy during the Directed Energy Deposition Arc Additive Manufacturing, *Crystals*, 2023, **13**(2), p 235.

33. M. Zheng, J. Yang, J. Xu, J. Jiang, H. Zhang, J.P. Oliveira, X. Lv, J. Xue, and Z. Li, Interfacial Microstructure and Strengthening Mechanism of Dissimilar Laser Al/Steel Joint Via a Porous High Entropy Alloy Coating, *J. Mater. Res. Technol.*, 2023, **23**(3997), p 4011.

34. F.B. Teshome, B. Peng, J.P. Oliveira, J. Shen, S. Ao, H. Li, L. Chen, C. Tan, X. Song, N. Zhou, and Z. Zeng, Role of Pd Interlayer on NiTi to Ti6Al4V Laser Welded Joints: Microstructural Evolution and Strengthening Mechanisms, *Mater. Des.*, 2023, **228**, p 111845.

35. V. Brailovski, S. Prokoshkin, K. Inaekyan, M. Petrzhik, M. Filonov, Y. Pustov, S. Dubinskiy, Y.S. Zhukova, A. Korotitskiy, and V. Sheremetyev, Thermomechanical Treatment of Ti-Nb Solid Solution Based SMA, *Mater. Sci. Found.*, 2015, **81**(342), p 405.

36. Y.S. Kim, H.J. Park, J.T. Kim, S.H. Hong, G.H. Park, J.M. Park, J.Y. Suh, and K.B. Kim, Influence of Nb on Microstructure and Mechanical Properties of Ti-Sn Ultrafine Eutectic Alloy, *Met. Mater. Int.*, 2017, **23**(20), p 25.

37. A.M. Omran, K.D. Woo, D.K. Kim, S.W. Kim, M.S. Moon, N.A. Barakat, and D.L. Zhang, Effect of Nb and Sn on the Transformation of α-Ti to β-Ti in Ti-35 Nb-2.5 Sn Nanostructure Alloys Using Mechanical Alloying, *Metals Mater. Int.*, 2008, **14**(321), p 325.

38. H.R. Jafarian, M. Sabzi, S.M. Anijdan, A.R. Eivani, and N. Park, The Influence of Austenitization Temperature on Microstructural Developments, Mechanical Properties, Fracture Mode and Wear Mechanism of Hadfield High Manganese Steel, *J. Market. Res.*, 2021, **10**(819), p 831.